Blind Color Decomposition of Histological Images

Milan Gavrilovic*, *Member, IEEE*, Jimmy C. Azar, Joakim Lindblad, Carolina Wählby, Ewert Bengtsson, *Senior Member, IEEE*, Christer Busch, and Ingrid B. Carlbom, *Member, IEEE*

***Abstract*—Cancer diagnosis is based on visual examination under a microscope of tissue sections from biopsies. But whereas pathologists rely on tissue stains to identify morphological features, automated tissue recognition using color is fraught with problems that stem from image intensity variations due to variations in tissue preparation, variations in spectral signatures of the stained tissue, spectral overlap and spatial aliasing in acquisition, and noise at image acquisition. We present a blind method for color decomposition of histological images. The method decouples intensity from color information and bases the decomposition only on the tissue absorption characteristics of each stain. By modeling the charge-coupled device sensor noise, we improve the method accuracy. We extend current linear decomposition methods to include stained tissues where one spectral signature cannot be separated from all combinations of the other tissues' spectral signatures. We demonstrate both qualitatively and quantitatively that our method results in more accurate decompositions than methods based on non-negative matrix factorization and independent component analysis. The result is one density map for each stained tissue type that classifies portions of pixels into the correct stained tissue allowing accurate identification of morphological features that may be linked to cancer.**

***Index Terms*—Blind source separation, gastrointestinal tract, image restoration, microscopy, prostate, quantification .**

I. Introduction

DETECTION, diagnosis, and severity-grading of cancer are based on visual examination under a microscope of histopathological sections from tissue biopsies. This practice is prone to subjectivity, resulting in significant variations between experienced pathologists. Studies show that inter- and intra-observer variations for prostate cancer grading can be as high as 30%–40% [1]. But quantitative tissue analysis based on automated image analysis has the potential to reduce or eliminate subjectivity in cancer diagnosis, yielding a more objective basis for a course of treatment. Quantitative tissue analysis also has a large potential role in research, allowing for rapid throughput of large amounts of histopathological data, as is required by for example the Human Protein Atlas Project [2].

Pathologists rely on multiple, contrasting stains for tissue analysis. For example hematoxylin, which stains cell nuclei blue, is usually combined with the counter-stain eosin that stains cytoplasm in pink and stromal components in various grades of red/pink, providing local color-contrast. But whereas pathologists can effectively use color in combination with texture and morphological features for visual analysis, automated tissue recognition based on color is fraught with problems. First, there can be large inter- and intra-specimen variations in stained tissue color due to tissue preparation factors, including variations in stain concentration, staining duration, tissue thickness, and in fixation. Tabesh *et al.* [3] argue that color does not contain much information regarding the severity grade (in prostate cancer) since intra-grade color variations are often greater than inter-grade color variations. In order to use color for severity grading, it is essential that tissue classification be based solely on the tissue absorption characteristics for a specific stain without the influence of variations that are introduced during specimen preparation [4].

A second set of problems is the result of aliasing in the image acquisition process, both in the spectral and spatial domains. Different stains may have overlapping absorption spectra, requiring a decomposition method that classifies portions of pixels into the correct tissue classes. Instead of classifying a pixel that contains two or more stained tissue types into only one type (binary classification), soft classification separates the relative contributions of the stained tissue to each pixel yielding a more accurate classification. Similarly, aliasing due to limited spatial resolution or tissue thickness may result in multiple tissue components, e.g., cell nuclei and cytoplasm, to be collocated within a single pixel. Again, for a more accurate classification, we need to separate the relative contributions of each stained tissue type within pixels.

A third problem is the result of noise at image acquisition. Standard three-channel charge-coupled device (CCD) sensors have a linear response to the number of incident photons and the dominant noise is Poisson-distributed photon noise [5], [6]. Introduction of noise modeling into the decomposition increases the accuracy of the results. Another type of noise is due to variations in the spectral signature of the stained tissue, i.e., color samples of the same tissue type stained with the same stain and with the same optical density can exhibit different spectral properties. In fluorescence microscopy this is sometimes referred to as biochemical noise [7].

Manuscript received September 24, 2012; revised December 25, 2012; accepted January 01, 2013. Date of publication January 11, 2013; date of current version May 29, 2013. This work was supported in part by the Swedish Research Council under Grant 2009-5418. *Asterisk indicates corresponding author.*

*M. Gavrilovic was with the Centre for Image Analysis of Uppsala University and Swedish University of Agricultural Sciences, S-75105 Uppsala, Sweden. He is now with HotSwap Engineering Consultants, S-17263 Stockholm, Sweden (e-mail: gavrilovic@ieee.org).

J. C. Azar, E. Bengtsson, and I. B. Carlbom are with the Centre for Image Analysis, Uppsala University and Swedish University of Agricultural Sciences, S-75105 Uppsala, Sweden.

J. Lindblad was with the Centre for Image Analysis, Uppsala University and Swedish University of Agricultural Sciences, S-75105 Uppsala, Sweden. He is now with the Faculty of Technical Sciences, University of Novi Sad, 21000 Novi Sad, Serbia.

C. Wählby is with the Centre for Image Analysis, Uppsala University and Swedish University of Agricultural Sciences, S-75105 Uppsala, Sweden and also with the Broad Institute of Harvard and MIT, Cambridge, MA 02142 USA.

C. Busch is with the Department of Immunology, Genetics and Pathology, Uppsala University, S-75185 Uppsala, Sweden.

Digital Object Identifier 10.1109/TMI.2013.2239655

Color decomposition is a technique developed in fluorescence microscopy based on ideas from remote sensing. Keshava and Mustard [8] describe spectral unmixing as a procedure requiring determination of reference spectra, or colors, and decomposition, i.e., the extraction of a set of gray-level images showing individual contributions of the pixels to each spectral band.

Whereas multispectral solutions offer the advantage that filters may be matched to several stained tissue types [9], multispectral imaging is more costly and more time consuming than three channel [red–green–blue (RGB)] imaging, which is the standard in bright-field microscopy. Reference [10] shows that multi-spectral imaging does not give a statistically significant increase in performance in histopathological image analysis. Therefore, we focus on RGB images, but the extension to multiple spectra is straightforward.

In this paper, we develop a new method, referred to as the Blind Color Decomposition (BCD) method, for stained tissue separation in transmission light microscopy based on the idea that intensity should be decoupled from color information. Unlike many existing solutions our method is blind, also sometimes referred to as unsupervised, i.e., it does not require input by the user in the form of training sets or special specimens to extract information prior to processing. We use statistical techniques for noise modeling of the CCD array and also devise a measure for biochemical noise. We assume that stains are light absorbing, as is generally the case, and model the relationship between the stain and its absorption using the Beer–Lambert law [11], [12]. We map the color information in the image to the Maxwellian color space and use pattern analysis techniques to estimate the stained tissue color, also known as the reference color.

Existing color decomposition techniques depend on the inversion of a color mixing matrix which requires that the reference colors are linearly independent in color space [13]. Moreover clusters around the reference colors (chromaticity clusters) need to be fully separable, that is both pair-wise separable and one-against-all separable, for the inversion of the color mixing matrix to give a good result [14]. However, when chromaticity clusters are pair-wise separable, but one of the clusters is not separable from all the others, we call the clusters partially separable (which is the case for trichrome stains such as Gomori trichrome [15], a stain that is used to separate smooth muscle and collagen). We extend current linear decomposition methods to include color clusters that are partially separable by dividing the inversion into a set of linear problems, and then inverting one color mixing matrix at a time. We refer to this as piece-wise linear decomposition.

The BCD method, as all linear decomposition methods, requires that the data be linearized using the Beer–Lambert Law of absorption, which applies only to light-absorbing stains. If a specimen contains stains that do not absorb light but rather scatter light [4], [12], as is the case for Diaminobenzidine (DAB), we suggest removal of the DAB-stained areas from the image prior to color decomposition.

The presentation of our color decomposition proceeds as follows. First we derive the theoretical underpinnings of a linear mixture model. This is followed by an algorithm to remove intensity variations by mapping the image data to the Maxwellian chromaticity plane. After the intensity variations are removed, we identify the reference colors and use these to formulate the decomposition rules. Section IV discusses methods that can improve blind decomposition by estimating noise in the image data and how to use this noise in a practical solution to the pattern classification problem which identifies the reference colors in the Maxwellian plane. In Section V, we show quantitative comparisons of our method with methods in the literature using large data sets of hematoxylin-and-eosin-stained (H&E) bladder neck and stomach tissue [16], and prostate tissue stained with hematoxylin-and-Herovici (H&H) [17], and with Giemsa-and-eosin (G&E) [18].

A first quantitative comparison using the relative root-mean-square errors (rRMSE) of the mixing matrices produced by independent component analysis (ICA), non-negative matrix factorization (NMF), BCD, and a ground truth mixing matrix as defined by an experienced pathologist reveals that our method outperforms NMF by between 20% and 40% and ICA at greater margins. A second quantitative comparison of the same methods using the Pearson correlation coefficient demonstrates that our density maps give on average a 91% median correlation with ground truth for the weaker stain eosin in H&E, compared to other published methods that give up to an 81% median correlation for eosin. For the less common stains, H&H and G&E, our density maps give a 98% median correlation with the ground truth for the weaker stain, compared to other published methods that give less than a 90% median correlation. In the case when the chromaticity clusters are only partially separable, our piecewise linear decomposition gives density maps with a median correlation of 95%, compared to 40% for linear decomposition. Qualitative comparisons support the quantitative results, clearly illustrating that our density maps yield results superior to those of published methods. We end with a few observations on stain quality and limitations of the BCD method.

II. Background and Related Work

Color decomposition methods in the literature differ in terms of the imaging sensor type employed, whether they model tissue light absorption or determine the reference color in color space, by the method of parameter estimation, and whether the result is a binary map indicating whether a stain is present in a pixel or not, a density map giving the proportion of a stained tissue in each pixel, or a probability map where each pixel indicates the probability of the presence of one stained tissue type versus other tissue types. Some reference color determination methods may require user input, whereas others are completely automated. Finally, only some methods handle partially separable reference color clusters.

Reference color determination in histological applications often relies on clustering techniques implemented directly in color space, without any consideration for stain–tissue interactions or sensors properties. Such methods [19], [20] result only in binary classification and do not give a quantitative density classification leading to "loss of information" [21].

Color deconvolution [21] is a decomposition method for transmission bright-field microscopy similar to Castleman's *color compensation* used in fluorescence microscopy [22]. In

TABLE I
OVERVIEW OF REFERENCE COLOR DETERMINATION METHODS

	Methods for color decomposition				
	Imaging sensor	Models absorption	Parameter Estimation	Resulting Maps	Decomposes part. separable clusters
[19]	Three-channel	No	Nearest Neighbor	Binary	Yes
[20]	Three-channel	No	Mean-shift and HNC	Binary	Yes
[21]	Three-channel	Yes	From single stained spec.	Density	No
[23]	Multi-spectral	No	ICA, NMF	Probability	No
[24]	Hyper-spectral	Yes	Relative Newton Method	Density	No
[25]	Three-channel	No	NMF	Probability	No
[26,3]	Three-channel	No	PCA	Probability	No
BCD	Three-channel	Yes	EM in chromaticity plane	Density	Yes

color deconvolution the relative absorption of the three channels are measured on slides with a single stain. This is followed by a transformation of the data by the Beer–Lambert law and the computation of normalized average RGB values for each selected tissue. These normalized color vectors are then used to build a mixing matrix for the decomposition of the color image into density images, one for each stained tissue type.

Blind methods, borrowed from remote sensing for determining reference spectra or tissue colors, are based on NMF, ICA, or principal component analysis (PCA), with the first two resulting in density maps and the last in a probability map. Reference [23] uses ICA and NMF to analyze multispectral data. Reference [24] shows excellent results for sparse hyperspectral data using PCA for dimensionality reduction followed by the relative Newton method, a blind source separation algorithm. This method relies on the number of wavelengths to exceed by at least two the number of stains present in the slide, and hence it is not applicable to three-channel data in histopathology. Only NMF [25] and PCA [26] have been tested using three-color image data.

Following decomposition, soft pixel classification is often implemented as a matrix multiplication by the pseudo inverse of the mixing matrix [8], [21], [25], [27] (note that the last reference deals with fluorescence microscopy). This requires all reference spectra or colors of the identified tissue types to be linearly independent, but it gives good decomposition results only when the stained tissues are fully separable.

Spectral angle mapping, often used in fluoresce microscopy [4], [28], [29], offers a stable solution even when the clusters around the reference color are only partially separable and it allows for a greater number of tissue types than color channels. However, the output images of spectral angle mapping are binary, that is the mapping does not use linear decomposition but rather nearest neighbor pixel classification by spectral angles. The major features of the referenced work are summarized in Table I.

In summary the BCD method 1) is blind, that is it does not require that the user manually identify individual stained tissue types, 2) it models absorption using the Beer–Lambert law, and 3) it results in density maps, one for each stained tissue type, for both fully and partially separable chromaticity clusters. These quantitative density maps can be further processed using well-known, grey-level image analysis techniques for extracting features, such as texture and shape [30]–[32].

III. METHODS FOR COLOR DECOMPOSITION

A. Notation

$\mathbf{c}(\mathbf{p})$ The color samples in $\mathbf{C}$, the input color image of a histological specimen, and $\mathbf{c}(\mathbf{p}) = [c_1(\mathbf{p})\ c_2(\mathbf{p})\ c_3(\mathbf{p})]^T$, where c_1, c_2, and c_3, denote the red–green–blue sample values at each spatial coordinate (pixel) $\mathbf{p}$.

$\mathbf{a}_j$ The reference color unit vectors (in L_1 space) for each of the $j = 1, \ldots, n$ stained tissue types. The contributions of the stained tissue types add to one.

$\hat{\mathbf{d}}(\mathbf{p})$ The estimated relative proportions of the stained tissue for $\mathbf{p}$ in the imaged histological specimen, $\hat{\mathbf{d}}(\mathbf{p}) = [\hat{d}_1(\mathbf{p}) \ldots \hat{d}_n(\mathbf{p})]^T$. Each density map $\hat{d}_j(\mathbf{p})$ indicates how much of the stained tissue j is present in pixel $\mathbf{p}$.

What follows is similar to the derivation of the optical density in [24], but for sensors with wide wavelength bandwidths, such as in three-channel RGB cameras. Note that we apply logarithmic and exponential functions to a vector element-wise.

B. Image Formation and Linearization by the Beer–Lambert Law

We denote the intensity of the light source in a microscope that illuminates a histological specimen by the continuous function $S(\lambda)$, where λ is the wavelength. The transfer function of the microscope is denoted by $\mathbf{F}(\lambda) = [F_1(\lambda)\ F_2(\lambda)\ F_3(\lambda)]^T$, where F_k, $k = 1, 2, 3$, are the transfer functions of the individual red–green–blue color channels, respectively. The spectral distribution of the measured light intensity is represented by the spectral signature $\varphi(\mathbf{p}, \lambda)$ over wavelengths λ ranging from $\lambda_{\min}$ to $\lambda_{\max}$ [33]. The color sample at each pixel, $\mathbf{c}(\mathbf{p})$, can be defined by the spectral signature and the transfer functions as

$$\mathbf{c}(\mathbf{p}) = \int_{\lambda_{\min}}^{\lambda_{\max}} \varphi(\mathbf{p}, \lambda)\mathbf{F}(\lambda)d\lambda. \quad (1)$$

The color distribution for an image (Fig. 1) is often visualized as a 3-D scatter plot (Fig. 2). This image is a stomach tissue section stained with Gomori Trichrome that is used for illustration purposes in this section; in later sections we demonstrate our method on several stains and tissue types including the Gomori trichrome-stained stomach tissue.

Most stain light absorption follows the Beer–Lambert law that describes the relationship between stain concentration and its absorption [11]. From the Beer–Lambert law it follows that

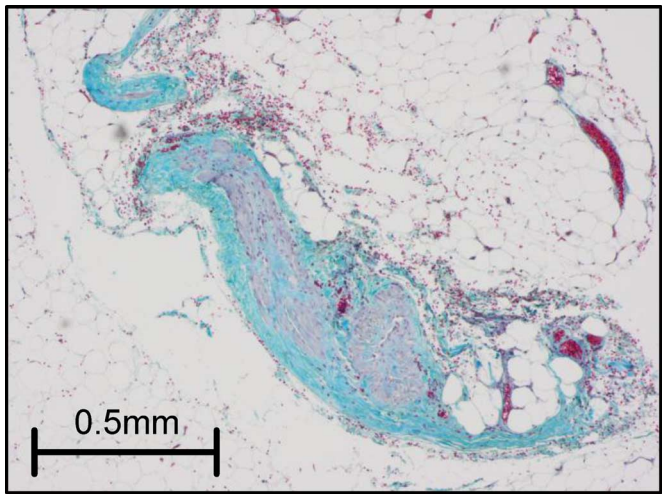

Fig. 1. An example of an input color image with $n = 3$ stained tissue types—a stomach section stained with Gomori trichrome. Erythrocytes appear as red, cell nuclei of fibroblasts and lymphocytes as purple, smooth muscle as grayish-purple, and collagen as turquoise.

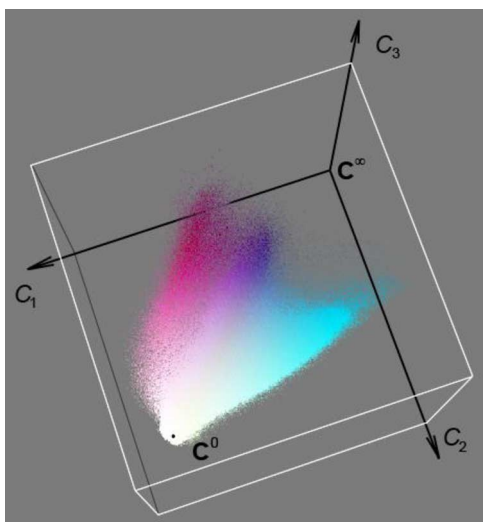

Fig. 2. Scatter-plots show the 3-D distribution in the red–green–blue color cube. This figure shows the scatter-plot of the input image $\mathbf{C}$ in Fig. 1.

the spectral signature for a specimen containing n light-absorbing stained tissue types is

$$\varphi(\mathbf{p}, \lambda) = S(\lambda) \exp\left(- \sum_{j=1}^{n} A_j(\lambda) d_j(\mathbf{p}) \right) \tag{2}$$

where $A_j(\lambda)$ is the absorption spectrum for the stained tissue j, and $d_j(\mathbf{p})$ is the total amount of stained tissue in pixel $\mathbf{p}$. From (1) and (2), we derive the intensities acquired in the individual color channels of $\mathbf{c}$

$$\mathbf{c}(\mathbf{p}) = \int_{\lambda_{\min}}^{\lambda_{\max}} S(\lambda) \exp\left(- \sum_{j=1}^{n} A_j(\lambda) d_j(\mathbf{p}) \right) \mathbf{F}(\lambda) d\lambda \tag{3}$$

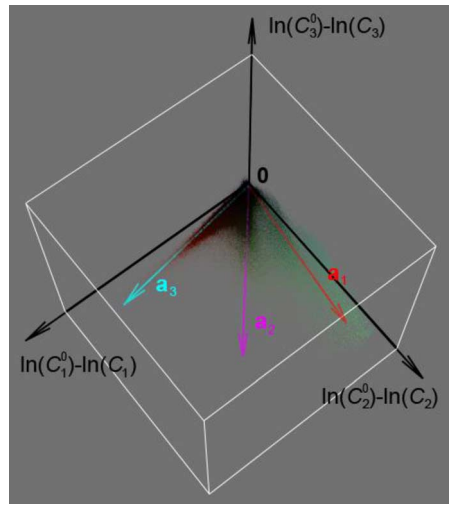

Fig. 3. Three-dimensional scatter plot of the Beer–Lambert-transformed input image $\mathbf{C}$ (shown in Fig. 1). Three reference color vectors $\mathbf{a}_1$, $\mathbf{a}_2$, and $\mathbf{a}_3$ are highlighted.

which can be rewritten as

$$\mathbf{c}(\mathbf{p}) = \int_{\lambda_{\min}}^{\lambda_{\max}} S(\lambda) \prod_{j=1}^{n} \exp\left(-A_j(\lambda) d_j(\mathbf{p})\right) \mathbf{F}(\lambda) d\lambda. \tag{4}$$

Fig. 2 shows that the color for each stained tissue, j, is clustered along an arc that starts at one end of the achromatic axis where no light is absorbed, i.e., $\mathbf{d}(\mathbf{p}^0) = \mathbf{0}$, which corresponds to the color of the illumination source

$$\mathbf{c}^0 \equiv \mathbf{c}(\mathbf{p}^0) = \int_{\lambda_{\min}}^{\lambda_{\max}} S(\lambda) \mathbf{F}(\lambda) d\lambda \tag{5}$$

and bends to the other end of the achromatic axis where the light source is fully attenuated, i.e., $d_j(\mathbf{p}^\infty) \to \infty$, $j = \{1, \ldots, n\}$, which corresponds to $\mathbf{c}^\infty \to \mathbf{0}$. According to the first mean value theorem, there exist n wavelengths for each channel k, such that $\lambda_{k,j} \in [\lambda_{\min}, \lambda_{\max}]$, transforming (4) into

$$c_k(\mathbf{p}) = \prod_{j=1}^{n} \exp(-A_j(\lambda_{k,j}) d_j(\mathbf{p})) \int_{\lambda_{\min}}^{\lambda_{\max}} S(\lambda) F_k(\lambda) d\lambda \tag{6}$$

which by using (5) becomes

$$c_k(\mathbf{p}) = \exp\left(- \sum_{j=1}^{n} A_j(\lambda_{k,j}) d_j(\mathbf{p}) \right) c_k^0. \tag{7}$$

Applying the logarithm to each side yields the optical density

$$\ln\left(c_k^0\right) - \ln(c_k(\mathbf{p})) = \sum_{j=1}^{n} A_j(\lambda_{k,j}) d_j(\mathbf{p}). \tag{8}$$

For each stained tissue type, the vectors on the left hand side of (8) belong to cone-like volumes centered about the vectors that define the reference colors in the scatter plot transformed by the Beer–Lambert law as seen in Fig. 3.

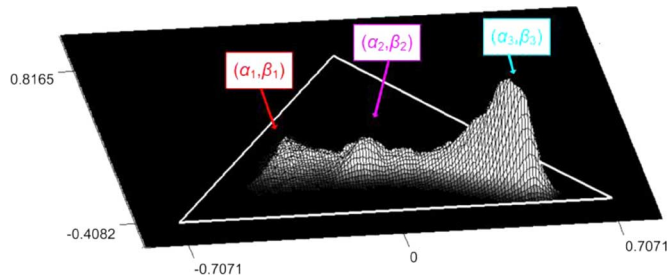

Fig. 4. The initial transformation of input RGB data $\mathbf{c}(\mathbf{p})$ is based on the Beer–Lambert law, followed by a perspective projection to the Maxwellian chromaticity plane. The three vertices are associated with the pure colors $[\ln(c_1^0)\ \ 0\ \ 0]^{\mathrm{T}}$, $[0\ \ln(c_2^0)\ \ 0]^{\mathrm{T}}$, and $[0\ \ 0\ \ \ln(c_3^0)]^{\mathrm{T}}$, which we refer to as Beer–Lambert red, green, and blue, respectively. (These colors correspond to cyan, magenta, and yellow in the original red–green–blue space.) The coordinates (α_1, β_1), (α_2, β_2), and (α_3, β_3) in the plane determine the three reference colors.

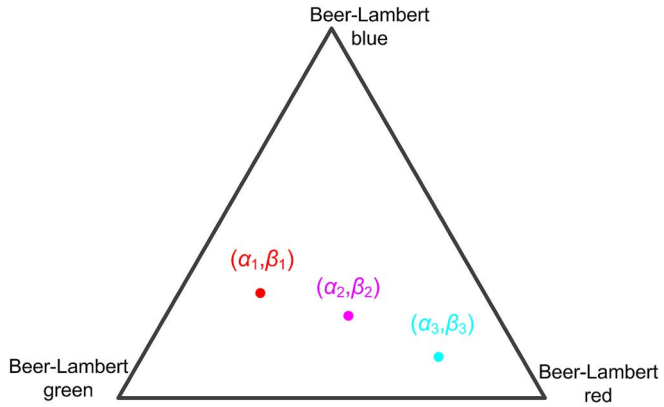

Fig. 5. Position of the three reference colors (α_j, β_j) in the Maxwellian chromaticity plane.

In the next section, we transform the input image data $\mathbf{C}$ to a pure color representation in the so called Maxwellian chromaticity plane, which allows pattern analysis techniques to identify the reference colors from the information contained in the image.

C. Maxwellian Chromaticity Plane

The Maxwell chromaticity plane or the Maxwell color triangle has the property that the distance between two points in the plane represents the chromaticity differences between the corresponding colors. Furthermore, pure RGB colors (in our case $[\ln(c_1^0)\ \ 0\ \ 0]^{\mathrm{T}}$, $[0\ \ln(c_2^0)\ \ 0]^{\mathrm{T}}$, and $[0\ \ 0\ \ \ln(c_3^0)]^{\mathrm{T}}$) project onto vertices of an equilateral triangle, and points on the achromatic axis (from $\mathbf{p}^{\infty}$ to $\mathbf{p}^0$) project to the triangle's circumcenter, at an equal distance from the three pure colors [34], [35].

The transformation from RGB-space to the Maxwellian chromaticity space can be expressed as a perspective transformation [36] with the center of projection at the origin $\mathbf{0}$ and the projection plane at the distance of $1/\sqrt{3}$ from the origin, yielding the following transformation:

$$\begin{bmatrix} \alpha(\mathbf{p}) \\ \beta(\mathbf{p}) \end{bmatrix} = \begin{bmatrix} \frac{1}{\sqrt{2}} & -\frac{1}{\sqrt{2}} & 0 \\ -\frac{1}{\sqrt{6}} & -\frac{1}{\sqrt{6}} & \sqrt{\frac{2}{3}} \end{bmatrix} \frac{\ln(\mathbf{c}^0) - \ln(\mathbf{c}(\mathbf{p}))}{\|\ln(\mathbf{c}^0) - \ln(\mathbf{c}(\mathbf{p}))\|_1} \tag{9}$$

where α and β are coordinates in the Maxwellian plane.

D. Reference Color Determination

The projected color data forms clusters in the Maxwellian chromaticity plane, with each cluster corresponding to one stained tissue type. Without knowledge about the exact data distribution, we assume that the clusters follow a Gaussian distribution with mean $(\alpha_j,\ \beta_j)$ [37]. The variances of the Gaussians are measures of the biochemical noise of the corresponding stained tissue types. In Fig. 4 we show the projected color data as a histogram over the Maxwellian color triangle, where the height indicates the number of color samples in the Beer–Lambert space at each coordinate in the Maxwellian plane; in Fig. 5 we show the reference colors in the Maxwellian chromaticity plane for the image data in Fig. 1.

Since we have no *a priori* knowledge about the shape and size of the clusters, we must rule out simpler methods, such as K-means and mean-shift for cluster identification. We rely on the Gaussian assumption and employ expectation maximization to find the clusters in the Maxwellian chromaticity plane. From the means of these Gaussian distributions, we calculate the reference color vectors using the inverse of (9), noting that the reference color vectors are unit vectors in L_1 space

$$\begin{aligned} a_{j,1} &= \sqrt{\frac{1}{2}}\alpha_j - \sqrt{\frac{1}{6}}\beta_j + \frac{1}{3} \\ a_{j,2} &= -\sqrt{\frac{1}{2}}\alpha_j - \sqrt{\frac{1}{6}}\beta_j + \frac{1}{3} \\ a_{j,3} &= 1 - a_{j,1} - a_{j,2}. \end{aligned} \tag{10}$$

We use the resulting reference color vectors, $\mathbf{a}_j$, to decompose the original image $\mathbf{C}$ into its density maps, as described in the following section.

E. Linear Decomposition

We use the reference color vectors $\mathbf{a}_j$ to blindly estimate the absorption spectra A_j in (8), up to a constant. Thus, we reformulate (8) in vector form as

$$\ln(\mathbf{c}^0) - \ln(\mathbf{c}(\mathbf{p})) = [\,\mathbf{a}_1 \quad \ldots \quad \mathbf{a}_n\,]\,\hat{\mathbf{d}}(\mathbf{p}) \tag{11}$$

where each $\mathbf{a}_j$ is a unit reference color vector, and contains the estimated *relative* proportions of the stained tissue.

We find the relative densities by solving (11) as a least-squares problem, the method known as linear decomposition. We multiply the optical density with the pseudo-inverse of the mixing matrix yielding the density maps

$$\hat{\mathbf{d}}(\mathbf{p}) = ([\mathbf{a}_1 \ldots \mathbf{a}_n]^T[\mathbf{a}_1 \ldots \mathbf{a}_n])^{-1}[\mathbf{a}_1 \ldots \mathbf{a}_n]^T(\ln(\mathbf{c}^0) - \ln(\mathbf{c}(\mathbf{p}))). \tag{12}$$

When one of the resulting elements of $\hat{\mathbf{d}}(\mathbf{p})$ is less than zero, the element is set to zero. This method of inversion assumes that the chromaticity clusters are fully separable.

When the chromaticity clusters are partially separable, that is when only one of the clusters (e.g., index j_2) has a poor one-

against-all cluster separation, i.e., poor separation with clusters j_1 and j_3, we use piece-wise linear decomposition. In this case we apply pseudo-inverse transformations of mixing submatrices, comprising reference color vectors j_2 and j_1, and j_2 and j_3, respectively. The two submatrices are multiplied with the optical density data and the results are combined to form the density map. The density map is defined by

$$\begin{aligned}\begin{bmatrix}\hat{d}'_{j_2}(\mathbf{p})\\ \hat{d}_{j_1}(\mathbf{p})\end{bmatrix} &= ([\mathbf{a}_{j_2}\mathbf{a}_{j_1}]^T[\mathbf{a}_{j_2}\mathbf{a}_{j_1}])^{-1}[\mathbf{a}_{j_2}\mathbf{a}_{j_1}]^T(\ln(\mathbf{c}^0)\\ &\quad - \ln(\mathbf{c}(\mathbf{p})))\\ \begin{bmatrix}\hat{d}''_{j_2}(\mathbf{p})\\ \hat{d}_{j_3}(\mathbf{p})\end{bmatrix} &= ([\mathbf{a}_{j_2}\mathbf{a}_{j_3}]^T[\mathbf{a}_{j_2}\mathbf{a}_{j_3}])^{-1}[\mathbf{a}_{j_2}\mathbf{a}_{j_3}]^T(\ln(\mathbf{c}^0)\\ &\quad - \ln(\mathbf{c}(\mathbf{p})))\\ \hat{d}_{j_2}(\mathbf{p}) &= \min(\hat{d}'_{j_2}(\mathbf{p}), \hat{d}''_{j_2}(\mathbf{p})). \qquad (13)\end{aligned}$$

The minimum in the third equation in (13) is motivated by the fact that choosing the decomposition (stain pair) which is best aligned with the observed color corresponds to selecting the decomposition where d_{j_1} or d_{j_3} has maximal density, i.e., d_{j_2} is minimal. Both the linear decomposition and the piece-wise linear decomposition result in quantitative density maps.

IV. Implementation

A. Overview

In contrast to supervised methods where an expert, e.g., a pathologist, provides a training set of reference colors [10] or sample regions [21], our approach automatically estimates the linear model parameters in (11) from the image data. Our method requires only the following minimal prior knowledge about the tissue specimen, 1) the number of light absorbing stained tissue types, n, and 2) a stored blank image from the microscope for measuring photon noise. Should the blank image not be available for the microscope, it can be estimated from the images.

Fig. 6 shows the processing pipeline from acquisition to the resulting density maps. For the bladder neck and stomach data we used an Olympus bright-field microscope for image acquisition; the microscope is accompanied by a CCD camera and $4\times/0.13$, $10\times/0.30$, and $20\times/0.50$ objectives, with standard red–green–blue optical filters. For the prostate data sets we used an Aperio ScanScope, model XT, with an Olympus Plan apochromatic $20\times/0.75$ objective.

The first step removes areas affected by light scattering stains. Next, we measure the photon noise parameters for modeling uncertainty in measured intensity values. This is followed by a transformation of the image data using the Beer–Lambert law of absorption, and a projection of the resulting data to the Maxwellian chromaticity plane, where we find n clusters. Thereafter, based on the means of these Gaussian-like clusters, (α_j, β_j), where $j = 1, \ldots, n$, we generate n reference color vectors that make up the columns of the mixing matrix, and apply linear decomposition to produce density maps.

All linear decomposition methods require that the data be linearized using the Beer–Lambert Law of absorption, which assumes that stained tissue absorb photons from the light source. However polymers, such as DAB, are commonly used in histopathology but they do not obey the Beer–Lambert law as they scatter rather than absorb light [4], [12]. We suggest removal of the DAB-stained areas from the image prior to color decomposition with standard image analysis techniques, so

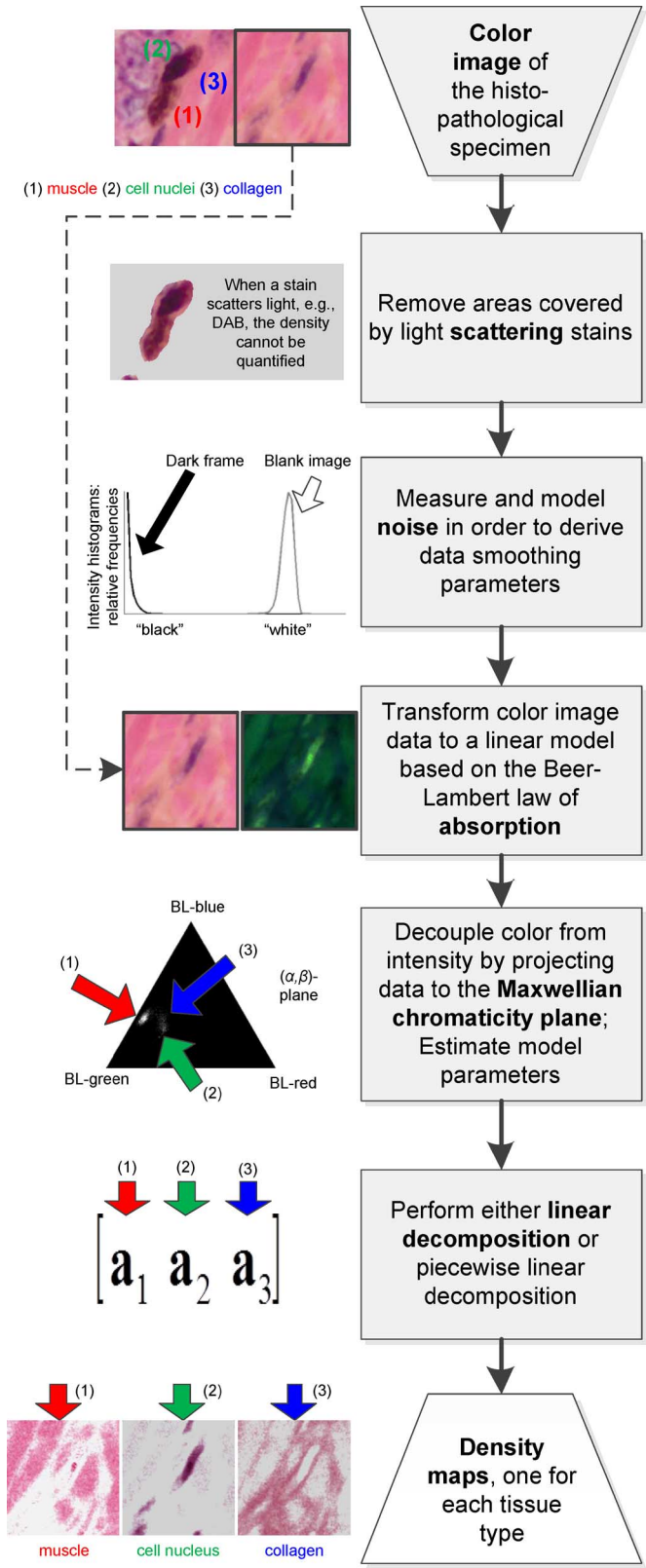

Fig. 6. Flowchart of the BCD method.

that the color decomposition will be based solely on the light absorbing stains.

B. The Noise Model

Standard three-channel CCD sensors have a linear response to the number of incident photons, and the dominant noise is Poisson-distributed photon noise [5], [6]. In the Maxwellian plane the areas with high optical density create distinct peaks with a high signal-to-noise ratio. The low optical density areas, on the other hand, tend to create spurious peaks, and the signal-to-noise level is low. As a result the photon noise has significant effect on these areas around "white." Accurate estimation of the noise parameters of the sensor can be used to smooth the data and to aid in the extraction of the distinct peaks corresponding to the reference colors.

The imaging device, that is the light source and the CCD array, is calibrated by acquiring a blank image and a dark frame. First, we use the blank image to automatically set the amplifier gains so that the image is perceived as "white." Second, we use these images to estimate the photon noise for any input color sample $\mathbf{c}(\mathbf{p})$. For each color channel k in the blank image, we derive the mean value of the intensities over the image, c_k^0, and their standard deviation, σ_k^0, from the intensity histogram for each channel. For the dark frame, the mean value of the measurements is set to be less than one quantization level, that is $c_k^\infty = 0$ [13]. However, due to the amplifier gain, the standard deviation, σ_k^∞, is generally not zero and can be estimated from the dark frame, also from the intensity histograms.

The standard deviations, σ_k, over all intensity levels c_k are derived by [5]

$$\sigma_k = \sqrt{(\sigma_k^\infty)^2 + \frac{(\sigma_k^0)^2 - (\sigma_k^\infty)^2}{c_k^0} c_k}. \tag{14}$$

Should the blank image and the dark frame not be available, we estimate σ_k^0 from the intensity histogram of a white area in the image, and set σ_k^∞ to the root mean square of the quantization noise. We make this assumption as precise noise measurements in very dark regions are not important due to the high signal-to-noise level. As shown in [38] the root mean square of the quantization noise becomes $\sigma_k^\infty = \sqrt{1/12}$.

In the next section, we show how to use the estimated noise parameters to smooth the image data.

C. Parameter Estimation

We use the noise model to aid in the parameter estimation. For each color sample $\mathbf{c}(\mathbf{p})$ present in the original image, we generate a cloud of N points $\mathbf{c}(\mathbf{p}_i), i = 1, \ldots N$, centered around $\mathbf{c}(\mathbf{p})$ in 3-D color space. Since only for high intensity values the noise has a significant effect on the transformation in (9), we approximate the 3-D Poisson distribution by a Gaussian distribution, with standard deviation $[\sigma_1 \ \sigma_2 \ \sigma_3]$ as derived in the previous section. All cloud points $\mathbf{c}(\mathbf{p}_i)$ are then transformed via the Beer–Lambert law, resulting in an increase in the number of points by a factor of N.

When selecting the reference colors, we give more weight to data with high optical density by assigning each point a score using a heuristic similar to that used in [29]

$$u(\mathbf{p}_i) = u_0 \cdot \max_{k=1,2,3} \left\{ \ln\left(c_k^0\right) - \ln(c_k(\mathbf{p}_i)) \right\} \tag{15}$$

where u_0 is a random variable drawn from a uniform distribution in [0,1], and $i = 1, \ldots, N$. Next, in order to reduce the number of data points back to the number of the original measurements, we retain $1/N$ of the points with highest scores. It is important to introduce randomization into the score when weighting the data points as is done in (15), otherwise the selection of the $1/N$ points with the greatest optical density values would be equivalent to intensity thresholding and would omit weaker stains such as eosin from the analysis. The next section shows that the noise model improves the solution with increasing N, until N reaches between five and seven and it does not improve the solution further up to $N = 20$. In all our experiments discussed below we set $N = 10$.

As described earlier, we use expectation maximization to fit Gaussian distributions to the color data in the Maxwellian plane. The mean values of these distributions allow us to estimate the reference color vectors that form the mixing matrix in the linear decomposition. The mixing matrices in (12) and (13) give the required density maps.

Separability of chromaticity clusters, whether they are fully separable or partially separable, determines whether a linear or piece-wise linear decomposition is applicable. One-against-one separability can be measured with statistical techniques, such as the Fisher criterion [14]. A high value of the Fisher criterion corresponds to clusters that are well separated, and lower Fisher criteria yield worse cluster separation. In the case of three stained tissue types, the clusters must be both one-against-one separable and one-against-all separable. In the case when there is one cluster that has a poor one-against-all separation to other clusters, but the others are fully separable, piece-wise linear decomposition will give a better decomposition result than simple linear decomposition.

V. Experimental Results

This section shows both quantitative and qualitative comparisons of the BCD method with existing methods for three tissue types and four different stains. We also demonstrate the importance of piecewise linear decomposition when stained tissue colors are only partially separable. We begin by describing how we acquire ground truth data.

A. Ground Truth and Validation

To produce ground truth data, we did not use the multiple histological staining method used in, for example [21] and [23], since most stains mix and also bind to the same tissue components, just in different degrees (this is not the case for DAB and hematoxylin, used in [21] and [23]). In other words ground truth data for H&E is hematoxylin in the presence of eosin, and vice versa. We demonstrate this by staining three adjoining prostate tissue sections with 1) hematoxylin alone, 2) eosin alone, and 3) both H&E, respectively. Our expert then picked in each of

TABLE II
REFERENCE COLOR VECTORS

	Stained tissue component (stain)					
	Nuclei (Htx)	Stroma (Htx)	Nuclei (Eosin)	Stroma (Eosin)	Nuclei (H&E)	Stroma (H&E)
$a_{j,1}$	0.38	0.33	0.11	0.07	0.34	0.20
$a_{j,2}$	0.42	0.43	0.58	0.62	0.46	0.55
$a_{j,3}$	0.20	0.24	0.31	0.31	0.20	0.25

the three sections 1) tissue that *should* be stained by hematoxylin (i.e., cell nuclei), and 2) tissue that *should* be stained by eosin (i.e., stroma). In Table II we show the reference color vectors that are the result of the decomposition of all three sections, hematoxylin alone, eosin alone, and H&E. We note that the reference color values particularly for eosin alone are different from the reference colors for the H&E combination. This demonstrates the necessity of selecting the ground truth using the combination of the stain components, as can be done only manually.

For our ground truth an experienced pathologist picked reference colors by selecting a number of pixels of each stained tissue type from a series of fields of view of each tissue. Please note that when the expert picked the stains, he did not use color as a guide but rather the morphological component that is known to be primarily stained, such as cell nuclei for hematoxylin. In what follows we use both the median of the pixels selected in each individual field of view (FOV ground truth) and also the median of all FOV values (total ground truth) as ground truth reference colors for that particular stained tissue, which make up the columns in ground truth mixing matrices.

B. Comparisons of Mixing Matrix Estimation Using rRMSE

Our first comparison of the BCD method with other methods in the literature is based on the relative rRMSE of the mixing matrices derived by ICA, NMF, and BCD as compared to the total ground truth mixing matrix. In all three cases the color image data is linearized using the Beer–Lambert law prior to the calculation of the mixing matrix. We also compute the rRMSE for the FOV ground truth mixing matrices as compared to the total ground truth mixing matrix to illustrate the variations in the ground truth over a tissue section. The rRMSE is derived by

$$\mathrm{rRMSE} = \sqrt{\frac{1}{N_{\mathrm{FOV}}} \sum_{l=1}^{N_{\mathrm{FOV}}} \frac{\|(\mathbf{a}^l - \mathbf{a}^{gt})^T(\mathbf{a}^l - \mathbf{a}^{gt})\|}{\sqrt{\|(\mathbf{a}^l)^T(\mathbf{a}^l)\| \cdot \|(\mathbf{a}^{gt})^T(\mathbf{a}^{gt})\|}}} \tag{16}$$

where $\mathrm{N_{FOV}}$ is the number of fields of view (in this experiment $\mathrm{N_{FOV}} = 23$), $\mathbf{a}^l$ is the estimated mixing matrix for the lth field of view, and $\mathbf{a}^{gt}$ is the total ground truth mixing matrix, and $\|\cdot\|$ denotes the matrix trace.

Table III shows the result for 21–23 (depending on tissue type) randomly chosen fields of view and reveals that our method outperforms NMF by between 20% and 40% and ICA with a much greater margin, for bladder neck tissue stained with H&E, stomach tissue stained with H&E, and prostate tissue stained with, H&H, and G&E, respectively. The row labeled "Pathologist" shows that the rRMSE for an expert is less than that for all the methods; the variations between stains can be attributed both to variations in stain quality over the sections and to minor errors by the expert.

TABLE III
RRMSE OF MIXING MATRIX ESTIMATION

	Tissue type (stain)			
Method	Bladder (H&E)	Stomach (H&E)	Prostate (H&H)	Prostate (G&E)
ICA	0.72	0.58	0.63	0.65
NMF	0.32	0.34	0.19	0.17
BCD	0.25	0.21	0.11	0.10
Pathologist	0.17	0.18	0.07	0.05

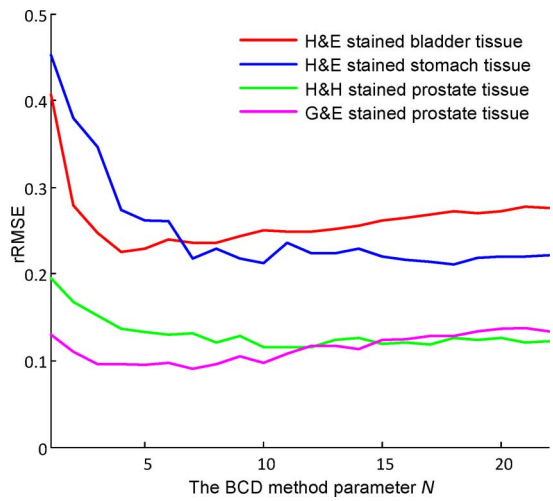

Fig. 7. The robustness with respect to the size of the point clouds, N, when the BCD method is applied to four different stained tissue types.

However, this comparison does not tell the whole story since an error in one reference color is partially transferred to the other color. Therefore, we need to also compare the resulting density maps, as is done in Section V-E below.

C. Noise Compensation Stability Tests

As discussed earlier, CCD noise modeling can improve the results of the parameter estimation. In Fig. 7 we show for each stained tissue type how the size of the point clouds that model the photon noise for each quantization level affects the rRMSE values. From $N = 1$ points, that is no noise model, the relative root-mean-square error improves with increasing N, until N reaches between five and seven, when the rRMSE levels off.

D. Qualitative Comparisons of BCD and NMF

Fig. 8 shows qualitative differences between the density maps from NMF (B, C) and the BCD (D, E) on one field of view of a prostate tissue section stained with H&H (A) (this field of view represents an average rRMSE of the whole tissue section). The visual results show a significant difference in, for example, the appearance of the nuclei (B and D), as a result of the bleed-through of the hematoxylin to the NMF eosin density map (C). We also notice bleed-through in the other direction for NMF; the stroma is not as well delineated in (C) as it is in (E), making a segmentation of the prostate gland easier from the BCD density map (E).

E. Comparisons Using the Pearson Correlation Coefficient

As we mentioned in an earlier section, a comparison based solely on mixing matrices does not tell the whole story, since

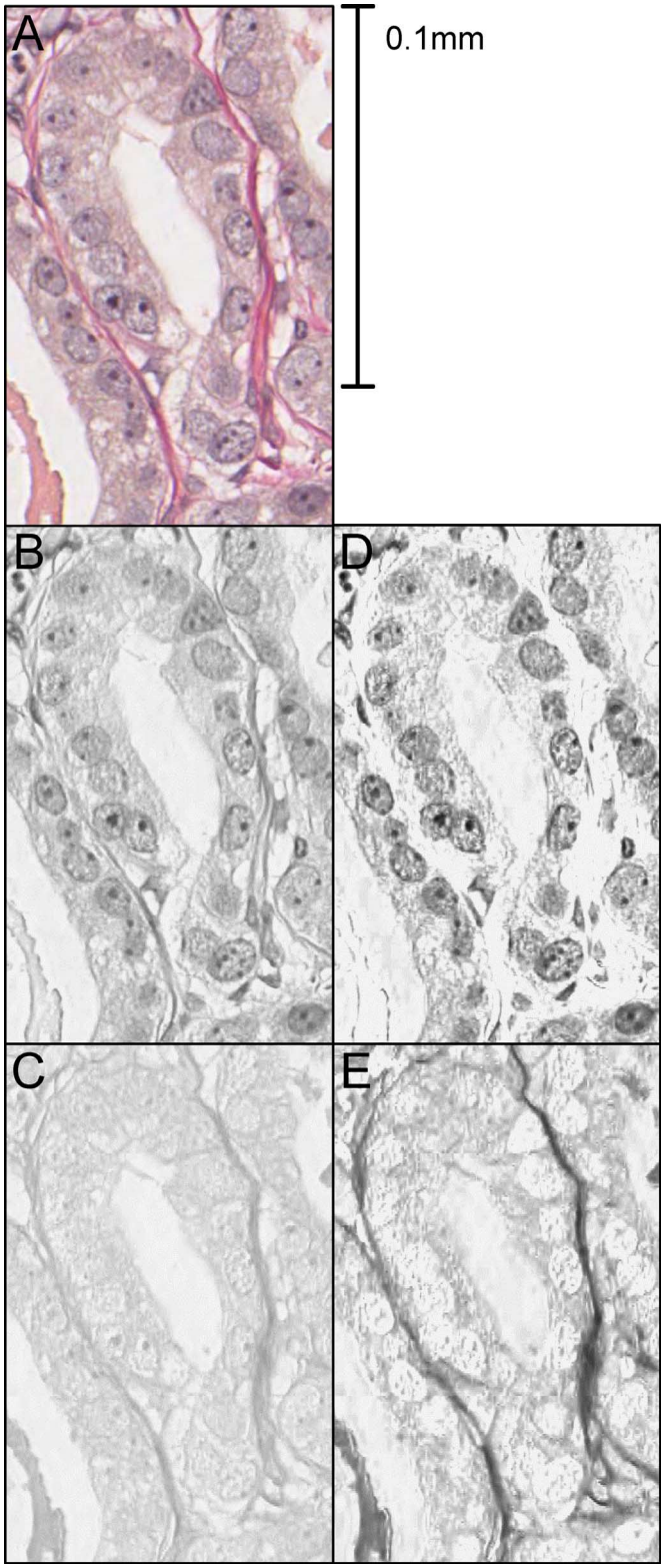

Fig. 8. Color decomposition of H&H stain (A) into density maps using NMF (B, C) and BCD (D, E).

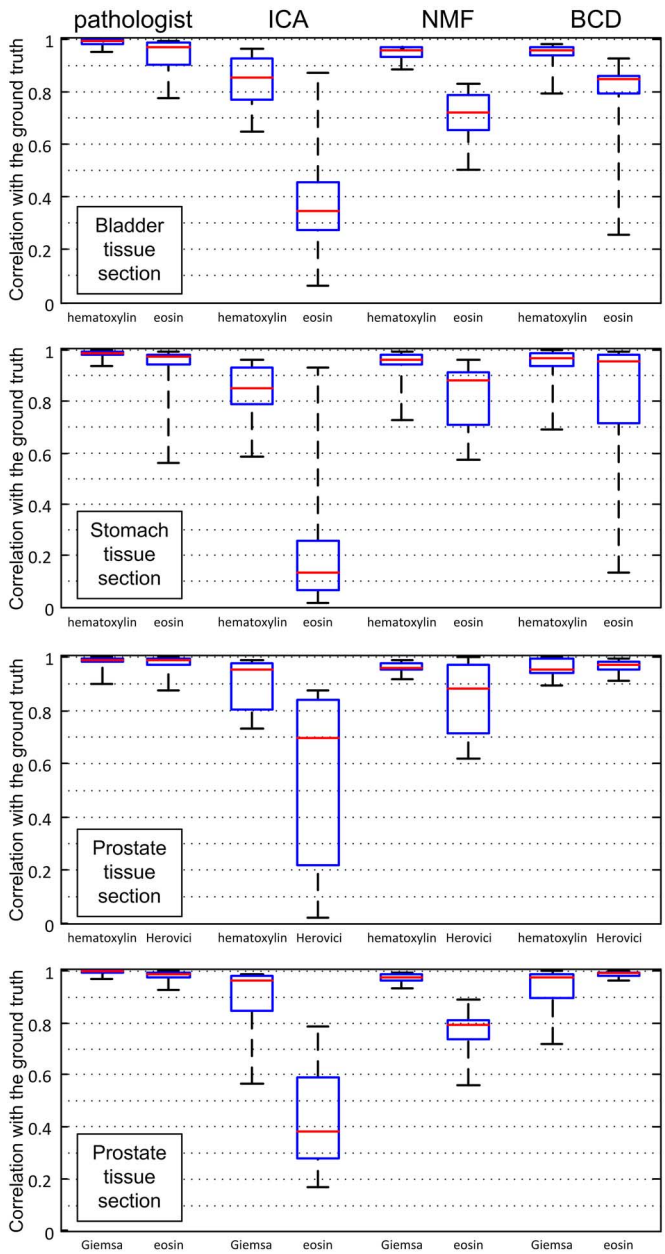

Fig. 9. Box plots with the results of comparisons of the BCD method and other blind methods implemented with identical preprocessing and linear decomposition. The density maps are derived by manual selection by a pathologist (pathologist), ICA, NMF, and color decomposition based on reference colors extracted from the Maxwellian chromaticity plane. The figure shows correlations for bladder neck tissue stained with H&E, stomach tissue stained with H&E, and prostate tissue stained with H&H, and G&E, respectively.

an error in estimation of one reference color vector is transferred to the other color (this was illustrated in the qualitative example above). Therefore, in this section we compare the resulting density maps for the identical tissue fields of view for the same stained tissue types as used in Section V-B above. The two comparisons combined give a complete analysis of our method as compared to other methods, both with regards to model parameter estimation and the significance of the estimation when the inverse model is applied to clinical data.

All the blind methods were randomly initialized and implemented with the same convergence criteria (residual changes by less than 10^{-4}), the number of iterations (1000), and number of replicates (one).

Fig. 9 shows Pearson correlation box plots of the ground truth density maps, with the density maps for the BCD method, ICA with assumed hyperbolic tangent non-Gaussian probability distribution function, and NMF. The experiment shows

that in these cases hematoxylin binds much better to the tissue than eosin, and the challenge for blind algorithms becomes to accurately detect eosin. Whereas all three methods identify the stronger stain, hematoxylin or Giemsa, only NMF and BCD give satisfactory results for the weaker stain, eosin or Herovici, with median correlations of 72% and 85%, respectively, for the bladder neck, and 88% and 96%, respectively, for the stomach tissue sections, 88% and 97%, respectively, for prostate tissue with Herovici, and 79% and 99%, respectively, for prostate tissue with eosin. The experimental results show that the median correlation for the BCD method performs better than both the other blind methods.

This evaluation method may also be suitable for correlating density maps with decomposition result derived by PCA. Its probability maps yielded the following median correlations for the weaker stains: 71% for the bladder neck tissue stained with H&E, 70% for the stomach tissue stained with H&E, 75% for the prostate tissue stained with H&H, and 90% for the prostate tissue stained with G&E. Thus we also conclude that PCA is outperformed by both NMF and BCD.

F. Validation of Piece-Wise Linear Decomposition

We also compared the difference between the two BCD decomposition strategies, linear decomposition and piece-wise linear decomposition, using identical reference color determination approaches. We generated the data for the comparison as follows.

1) The pathologist picked the reference colors for all three stained tissue types in 16 fields of view in the same manner as for other ground truth data, which resulted in a mixing matrix.
2) We perform a standard linear decomposition with all three stained tissue types using this mixing matrix.
3) We perform a piece-wise linear decomposition, according to (13), also using this mixing matrix.

In Fig. 10 we show the qualitative differences between two decompositions of stomach tissue sections stained by Gomori trichrome; in the left column the result from linear decomposition and in the right column from piece-wise linear decomposition. It is easy to see that the piece-wise linear decomposition gives more accurate density maps in particular for separation of collagen and connective tissue cells (fibroblasts).

To make a quantitative comparison of the same data, we must choose sections where the linear decomposition will give a correct answer, that is on fields of view that contain only two stained tissue types, in this case cell nuclei and collagen. The selected fields of view yield density maps that act as the ground truth in this quantitative comparison (we did not select erythrocytes as one of the tissue types since they are few and spatially separable).

In Fig. 11 the comparison between the density maps produced by linear and piece-wise linear decomposition using Pearson Correlation Coefficients shows a difference in median correlation to ground truth of 35% and 80% for collagen and cell nuclei, respectively. The statistical comparisons in Fig. 11 support the very large difference in the qualitative comparisons in Fig. 10.

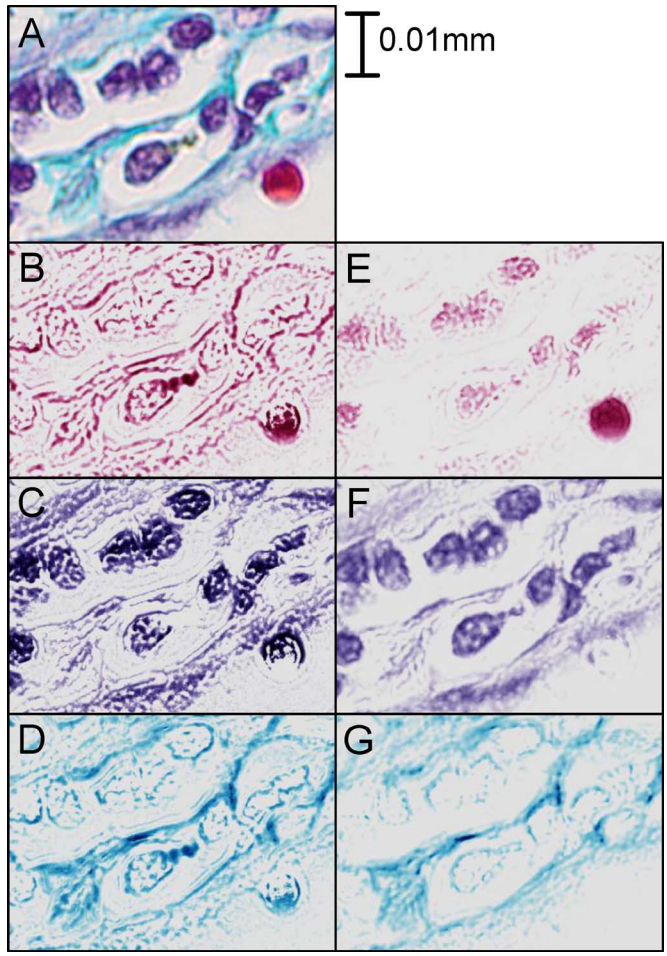

Fig. 10. Pseudo colored result of decomposition of Gomori trichrome stain (A) to density maps using: in B, C, and D linear decomposition, and in E, F, and G piece-wise linear decomposition rules. In B and E erythrocytes appear red, and in C and F cell nuclei of fibroblasts, lymphocytes and smooth muscle are purple, and in D and G collagen is turquoise.

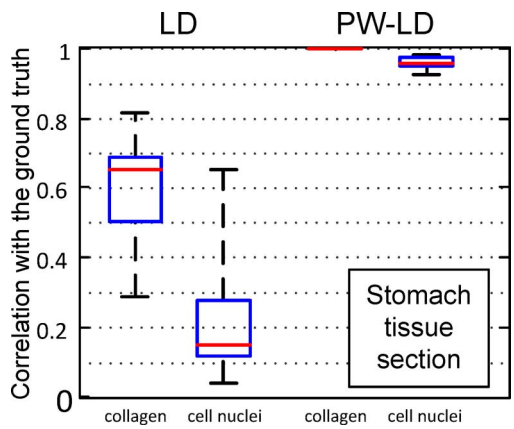

Fig. 11. Box plot with the results of the comparisons of the linear decomposition (LD) and piece-wise linear decomposition (PW-LD) to ground truth for 16 fields of view of stomach tissue sections stained with Gomori trichrome.

VI. Discussion and Conclusion

In this paper, we describe a blind method for color decomposition of histopathological tissue images based on a physical model of light absorption. We have demonstrated quantitatively

that in comparison to other blind methods, BCD gives better results when the stained tissues are fully separable. BCD, in contrast to other blind methods, also works for partially separable trichrome stains, such as Gomori trichrome.

We observed that Poisson noise is particularly dominant near "white" regions, where stain concentrations are low, as can be seen around $\mathbf{c}^0$ in Fig. 2. On the other hand, at high concentrations, towards $\mathbf{c}^\infty$, the dominant source of variation is biochemical noise [7]. It originates from variations in spectral signatures of stains.

The transformation of color samples to the Maxwellian chromaticity plane allows us to describe a perfect stain from a color theory point of view: its reference colors are compact, separable, and all tissue types absorb a similar amount of stain (no oversaturation, no weak stains). In addition to enabling quantification of stain quality by measuring the distance between reference colors in the Maxwellian chromaticity plane, we noticed the following:

1) variances of detected Gaussian distributions represent a measure of biochemical noise for each stained tissue type;
2) the Fisher separation criterion can measure stain quality.

The BCD method has some shortcomings: it fails, as do other blind methods, if a stain is not present in the image data, or the stain absorption is poor, and thus specimen preparation and imaging artifacts may obscure the estimation. The BCD method, as other linear decomposition methods, applies only to light absorbing stains. Polymers scatter light rather than absorb light and hence do not obey the Beer–Lambert law, and darkly stained DAB has a different spectral signature than lightly stained DAB [12]. Therefore, we suggest the removal of areas affected by light scattering stains with morphological techniques prior to the use of BCD [39].

The highly accurate density maps that result from the BCD method lend themselves to further processing using well-known, grey-level image analysis techniques for extracting morphological features, such as texture and shape that are known to distinguish cancer from normal tissue [40].

ACKNOWLEDGMENT

The authors would like to thank U. A. Larsson at the Uppsala University Hospital for preparing the tissue samples. The authors are also grateful to V. Curic at the Centre for Image Analysis, Uppsala University, for valuable discussions on the linear mixture models, and T. Marzetta at Bell Laboratories, NJ, for his help with the statistical analysis.

REFERENCES

[1] J. I. Epstein, W. C. Allsbrook, Jr., M. B. Amin, and L. Egevad, "Update on the Gleason grading system for prostate cancer: Results of an international consensus conference of urologic pathologists," *Adv. Anat. Pathol.*, vol. 13, no. 1, pp. 57–59, Jan. 2006.

[2] M. Uhlen, P. Oksvold, L. Fagerberg, E. Lundberg, K. Jonasson, M. Forsberg, M. Zwahlen, C. Kampf, K. Wester, H. Wernerus, L. Björling, and F. Ponten, "Towards a knowledge-based Human Protein Atlas," *Nature Biotech.*, vol. 28, pp. 1248–1250, 2010.

[3] A. Tabesh, M. Teverovskiy, H. Pang, V. P. Kumar, D. Verbel, A. Kotsianti, and O. Saidi, "Multifeature prostate cancer diagnosis and Gleason grading of histological images," *IEEE Trans. Med. Imag.*, vol. 26, no. 10, pp. 1366–1378, Oct. 2007.

[4] Y. Garini, I. T. Young, and G. McNamara, "Spectral imaging: Principles and applications," *Cytometry Part A.*, vol. 69A, pp. 735–747, Aug. 2006.

[5] J. C. Mullikin, L. J. van Vliet, H. Netten, F. R. Boddeke, G. van der Feltz, and I. T. Young, "Methods for CCD camera characterization," *Proc. SPIE Image Acquis. Sci. Imag. Syst.*, vol. 2173, pp. 73–84, 1994.

[6] G. Polder and G. W. van der Heijden, "Calibration and characterization of spectral imaging systems," *Proc. SPIE Multisp. Hypersp. Image Acquis.*, vol. 4548, pp. 10–17, 2001.

[7] K. R. Castleman, R. Eils, L. Morrison, J. Piper, K. Saracoglu, M. A. Schulze, and M. R. Speicher, "Classification accuracy in multiple color fluorescence imaging microscopy," *Cytometry*, vol. 41, no. 2, pp. 139–147, Sept. 2000.

[8] N. Keshava and J. F. Mustard, "Spectral unmixing," *IEEE Signal Process. Mag*, vol. 19, no. 1, pp. 44–57, Jan. 2002.

[9] R. M. Levenson, "Spectral imaging perspective on cytomics," *Cytometry Part A*, vol. 69A, pp. 592–600, Jul. 2006.

[10] L. E. Boucheron, Z. Bi1, N. R. Harvey, B. Manjunath, and D. L. Rimm, "Utility of multispectral imaging for nuclear classification of routine clinical histopathology imagery," *BMC Cell Biol.*, vol. 8, no. S8, Jul. 2007.

[11] W. W. Parson, *Modern Optical Spectroscopy*, 2nd ed. Berlin-Heidelberg, Germany: Springer, 2009, pp. 3–26.

[12] C. M. van der Loos, "Multiple immunoenzyme staining: Methods and visualizations for the observation with spectral imaging," *J. Histochem. Cytochem.*, vol. 56, no. 4, pp. 313–328, Apr. 2008.

[13] Q. Wu, F. Merchant, and K. Castleman, *Microscope Image Processing*, 1st ed. New York: Academic, 2008, pp. 299–323.

[14] A. Webb, *Statistical Pattern Recognition*, 2nd ed. Chichester, U.K.: Wiley, 2002, pp. 124–158, 362–370.

[15] G. Gömöri, "A rapid one-step trichrome stain," *Am. J. Clin. Pathol.*, vol. 20, no. 7, pp. 661–664, July 1950.

[16] M. Gamble, "The Hematoxylins and Eosin," in *Theory and Practice of Histological Techniques*, J. D. Bancroft and M. Gamble, Eds., 6th ed. Philadelphia, PA: Churchill Livingston Elsevier, 2008, pp. 121–134.

[17] C. Herovici, "A polychrome stain for differentiating precollagen from collagen," *Biotechnic Histochemistry*, vol. 38, no. 3, pp. 204–206, 1963.

[18] G. Giemsa, " Eine Vereinfachung und Vervollkommnung meiner Methylenazur-Methylenblau-Eosin-Färbemethode zur Erzielung der Romanowsky-Nocht'schen Chromatinfärbung," *Centralblatt für Bakteriologie*, vol. 37, pp. 308–311, 1904.

[19] K. Nguyen, A. K. Jain, and R. L. Allen, "Automated gland segmentation and classification for Gleason grading of prostate tissue images," in *Proc. 20th Int. Conf Pattern Recognit.*, 2010, pp. 1497–1500.

[20] A. Janowczyk, S. Chandran, R. Singh, D. Sasaroli, G. Coukos, M. D. Feldman, and A. Madabhushi, "Hierarchical normalized cuts: Unsupervised segmentation of vascular biomarkers from ovarian cancer tissue microarrays," *Med. Image Comput. Comput. Assist. Interv.*, vol. 12, no. 1, pp. 230–238, 2009.

[21] A. C. Ruifrok and D. A. Johnston, "Quantification of histochemical staining by color deconvolution," *Anal Quant. Cytol. Histol.*, vol. 23, no. 4, pp. 291–299, Aug. 2001.

[22] K. R. Castleman, "Concepts in imaging and microscopy: Color image processing for microscopy," *Biol. Bull.*, vol. 194, pp. 100–107, Apr. 1998.

[23] A. Rabinovich, S. Agarwal, C. Laris, J. H. Price, and S. Belongie, "Unsupervised color decomposition of histologically stained tissue samples," *Proc. Adv. Neur. Info. Process. Syst.*, pp. 667–674, 2003.

[24] G. Begelman, M. Zibulevsky, E. Rivlin, and T. Kolatt, "Blind decomposition of transmission light microscopic hyperspectral cube using sparse representation," *IEEE Trans. Med. Imag.*, vol. 28, no. 8, pp. 1317–1324, Aug. 2009.

[25] J. Newberg and R. F. Murphy, "A framework for the automated analysis of subcellular patterns in Human Protein Atlas images," *J. Proteome Res.*, vol. 7, no. 6, pp. 2300–2308, Jun. 2008.

[26] A. Tabesh and M. Teverovskiy, "Tumor classification in histological images of prostate using color texture," in *Proc. 40th Asilomar Conf. Signals, Syst. Comput.*, 2006, pp. 841–845.

[27] H. Choi, K. R. Castleman, and A. Bovik, "Color compensation of multicolor FISH images," *IEEE Trans. Med. Imag.*, vol. 28, no. 1, pp. 129–136, Jan. 2009.

[28] F. A. Kruse, A. B. Lefkoff, J. W. Boardman, K. B. Heidebrecht, A. T. Shapiro, P. J. Barloon, and A. F. H. Goetz, "The spectral image processing system (SIPS)—Interactive visualization and analysis of imaging spectrometer data," *Remote Sens. Environ.*, vol. 44, no. 2–3, pp. 145–163, Aug. 1993.

[29] M. Gavrilovic and C. Wählby, "Quantification of colocalization and cross-talk based on spectral angles," *J. Microscopy*, vol. 234, no. 3, pp. 311–324, June 2009.
[30] B. Nielsen, F. Albregtsen, and H. E. Danielsen, "Statistical nuclear texture analysis in cancer research: A review of methods and applications," *Crit. Rev. Oncog.*, vol. 14, no. 2–3, pp. 89–164, 2008.
[31] I. T. Young, P. W. Verbeek, and B. H. Mayall, "Characterization of chromatin distribution in cell nuclei," *J. Cytometry*, vol. 7, no. 5, pp. 467–474, Sept. 1986.
[32] N. Sladoje and J. Lindblad, "High-precision boundary length estimation by utilizing gray-level information," *IEEE Trans. Pattern Anal. Mach. Intell.*, vol. 31, no. 2, pp. 357–363, Feb. 2009.
[33] A. Koschan and M. Abidi, *Digital Color Image Processing*, 1st ed. Hoboken, NJ: Wiley, 2008, pp. 71–96.
[34] J. C. Maxwell, "On the theory of compound colours, and the relations of the colours of the spectrum," *Phil. Trans. R. Soc. Lond.*, vol. 150, pp. 57–84, Jan. 1860.
[35] D. E. Judd, "A Maxwell triangle yielding uniform chromaticity scales," *J. Opt. Soc. Am.*, vol. 25, no. 1, pp. 24–35, 1935.
[36] J. Foley, A. van Dam, S. Feiner, and J. Hughes, *Computer Graphics: Principles and Practice*, 2nd ed. Reading, MA: Addison-Wesley, 1996, pp. 213–281, in C.
[37] P. Stoica and P. Babu, "The Gaussian data assumption leads to the largest Cramér-Rao bound," *IEEE Signal Process. Mag.*, vol. 28, no. 3, pp. 132–133, May 2011.
[38] A. Gersho and R. M. Gray, *Vector Quantization and Signal Compression*, 1st ed. Norwell, MA: Kluwer, 1992, pp. 133–171.
[39] P. Soille, *Morphological Image Analysis, Principles and Applications*, 2nd ed. Berlin, Germany: Springer, 2004.
[40] M. B. Amin, D. J. Grignon, P. A. Humphrey, and J. R. Srigley, *Gleason Grading of Prostate Cancer*, 1st ed. Philadelphia, PA: Lippincott Williams Wilkins, 2004.